Supporting Information

Oxygen-Vacancy-Rich Fe_3O_4/Carbon Nanosheets Enabling High-Attenuation and Broadband Microwave Absorption through the Integration of Interfacial polarization and Charge-Separation polarization

Zhe Su,[a] Wanyu Zhang,[a] Jiawei Lu,[a] Liying Tian,[a] Shan Yi,[a] Yayun Zhang,[a] Shenghu Zhou,[a] Bo Niu,[a] and Donghui Long*[a]*

[a] Shanghai Key Laboratory of Multiphase Materials Chemical Engineering, East China University of Science and Technology, School of Chemical Engineering, Shanghai 200237, P. R. China.

* Corresponding authors.

Tel: +86 21 64252263.

Fax: +86 21 64252263.

E-mail address:

niubo@ecust.edu.cn (Bo Niu)

longdh@mail.ecust.edu.cn (Donghui Long)

According to the transmission line theory, the values of RL are calculated via the following equations:[1]

$$R_L(dB) = 20log\left|\frac{Z_{in} - Z_0}{Z_{in} + Z_0}\right| \quad \textbf{Equation S1}$$

$$Z_{in} = Z_0\sqrt{\frac{\mu_r}{\varepsilon_r}}tanh\left[j\frac{2\pi}{c}\sqrt{\mu_r\varepsilon_r}fd\right] \quad \textbf{Equation S2}$$

where Z_0 is the impedance of free space, Z_{in} is the normalized input impedance of the absorber, ε_r ($\varepsilon_r=\varepsilon' - j\varepsilon''$) is the relative complex permittivity of the absorber, μ_r ($\mu_r=\mu' - j\mu''$) is the relative complex permeability, f represents the electromagnetic wave frequency, c is the velocity of the EM wave in free space, and d expresses the thickness of the absorber, respectively.

Debye dipolar relaxation (Cole-Cole model), where the permittivity can be described as:[2]

$$\varepsilon_r = \varepsilon^{'} - j\varepsilon^{''} = \varepsilon_\infty + \frac{\varepsilon_S - \varepsilon_\infty}{1 + j2\pi f\tau} \qquad \textbf{Equation S3}$$

where τ, ε_s, ε_∞, and f stands for the polarization relaxation time, static permittivity constant, relative dielectric permittivity at the infinite frequency, and frequency, respectively. And then ε' and ε'' can be deduced as follows:

$$\varepsilon^{'} = \varepsilon_\infty + \frac{\varepsilon_S - \varepsilon_\infty}{1 + (2\pi f\tau)^2} \qquad \textbf{Equation S4}$$

$$\varepsilon^{''} = \varepsilon_\infty + \frac{2\pi f\tau(\varepsilon_S - \varepsilon_\infty)}{1 + (2\pi f\tau)^2} \qquad \textbf{Equation S5}$$

Based on above equations, the relationship between ε' and ε'' can be written as:

$$\left(\varepsilon^{'} - \frac{\varepsilon_S + \varepsilon_\infty}{2}\right)^2 + \left(\varepsilon^{''}\right)^2 = \left(\frac{\varepsilon_S - \varepsilon_\infty}{2}\right)^2 \qquad \textbf{Equation S6}$$

The eddy current can be calculated by the following eddy equation:[3]

$$c_0 = \mu^{''}\left(\mu^{'}\right)^{-2}(f)^{-1} = 2\pi\mu_0 d^2\sigma/3 \qquad \textbf{Equation S7}$$

where μ_0 and σ are the permeability of vacuum and the electric conductivity, respectively.

The attenuation constant α determines the dissipation properties of the material. It can be evaluated through the following equation:[2]

$$\alpha = \frac{\sqrt{2}\pi f}{c} \times \sqrt{(\mu''\varepsilon'' - \mu'\varepsilon') + \sqrt{(\mu''\varepsilon'' - \mu'\varepsilon')^2 + (\mu'\varepsilon'' + \mu''\varepsilon')^2}} \quad \textbf{Equation S8}$$

Delta values (Δ) therein can be deduced by the following equations,[2]

$$|\Delta| = |sinh^2(Kfd) - M| \quad \textbf{Equation S9}$$

where *K* and *M* can be determined by the relative complex permittivity and permeability via following equation,

$$K = \frac{4\pi\sqrt{\mu'\varepsilon'} \cdot sin(\frac{\delta_e + \delta_m}{2})}{c \cdot cos\delta_e \cdot cos\delta_m} \quad \textbf{Equation S10}$$

$$M = \frac{4\mu'\varepsilon' cos\delta_e cos\delta_m}{(\mu' cos\delta_e - \varepsilon' cos\delta_m)^2 + \left[tan\left(\frac{\delta_m}{2} - \frac{\delta_e}{2}\right)\right]^2 (\mu' cos\delta_e + \varepsilon' cos\delta_m)^2} \quad \textbf{Equation S11}$$

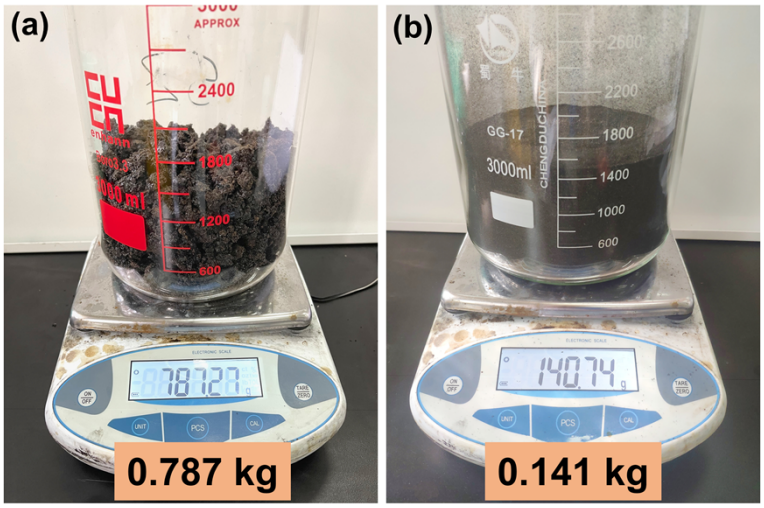

Figure S1. The digital photographs of a) mass-produced GlcA-Fe^{3+} precursors with a weight of 0.787 kg, b) 0.141 kg Fe_3O_4/C composites which are manufactured by annealing 0.413 kg GlcA-Fe^{3+} precursors in a big furnace at 700 °C for one hour.

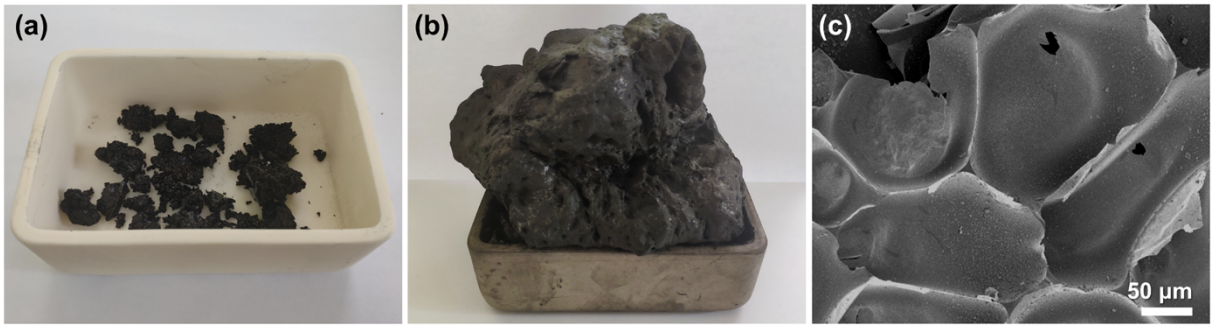

Figure S2. The digital photographs of a) GlcA-Fe^{3+} precursor and b) Fe_3O_4/C products. c) Low-resolution SEM image of honeycomb structured Fe_3O_4/C bulks.

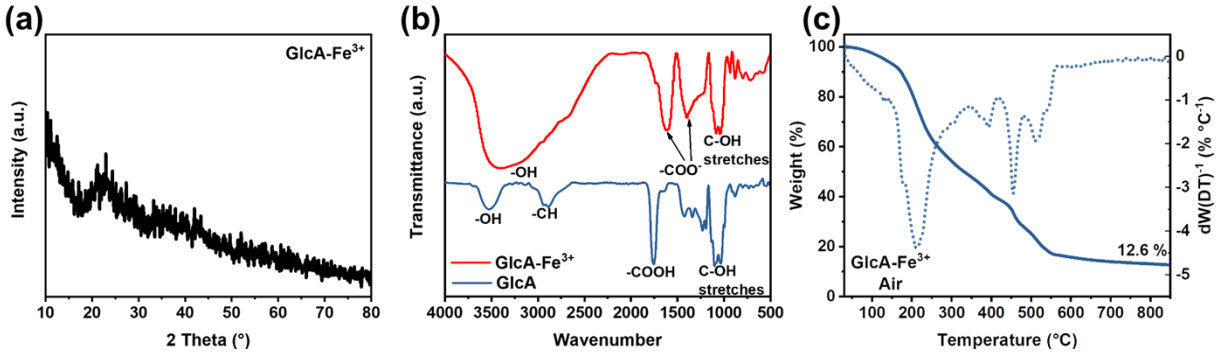

Figure S3. a) X-ray diffraction (XRD) pattern of GlcA-Fe^{3+} precursor. b) FT-IR spectra comparison between the GlcA-Fe^{3+} precursor and gluconic acid (GlcA). c) Thermogravimetric analysis (TGA) curve and derivative thermogravimetric (DTG) curve of GlcA-Fe^{3+} precursor under air atmosphere.

The FT-IR spectra of GlcA-Fe^{3+} shows that two intensive bands at 1585 cm^{-1} and 1385 cm^{-1} are the results of valence asymmetric and symmetric stretching vibrations of a carbonyl group (C=O) of carboxylate anion ($-COO^-$) (**Figure S3b**).[4] As a contrast, an isolated band located at 1755 cm^{-1} in the spectrum of gluconic acid (GlcA) is associated with the carbonyl group of carboxylic acid (-COOH).[5] Therefore, the difference in valence vibrations of carboxyl group indicates a coordination of gluconate anion and iron (III) ion in GlcA-Fe^{3+}.

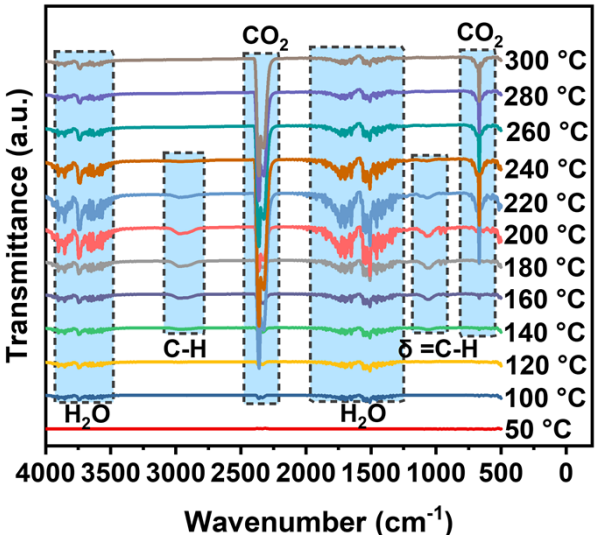

Figure S4. In-situ FT-IR spectra of pyrolysis gas evolved during the pyrolysis process of the GlcA-Fe^{3+} precursor.

Typical transmission bands for CO_2 are located at 2300 cm^{-1} corresponding to the asymmetric stretching mode, and bending vibration bands are located at 670 cm^{-1}. For gaseous water, two broad bands at around 1600 cm^{-1} (bending mode of H_2O) and 3600 cm^{-1} (symmetric and antisymmetric stretching mode of H_2O) are visible.[6]

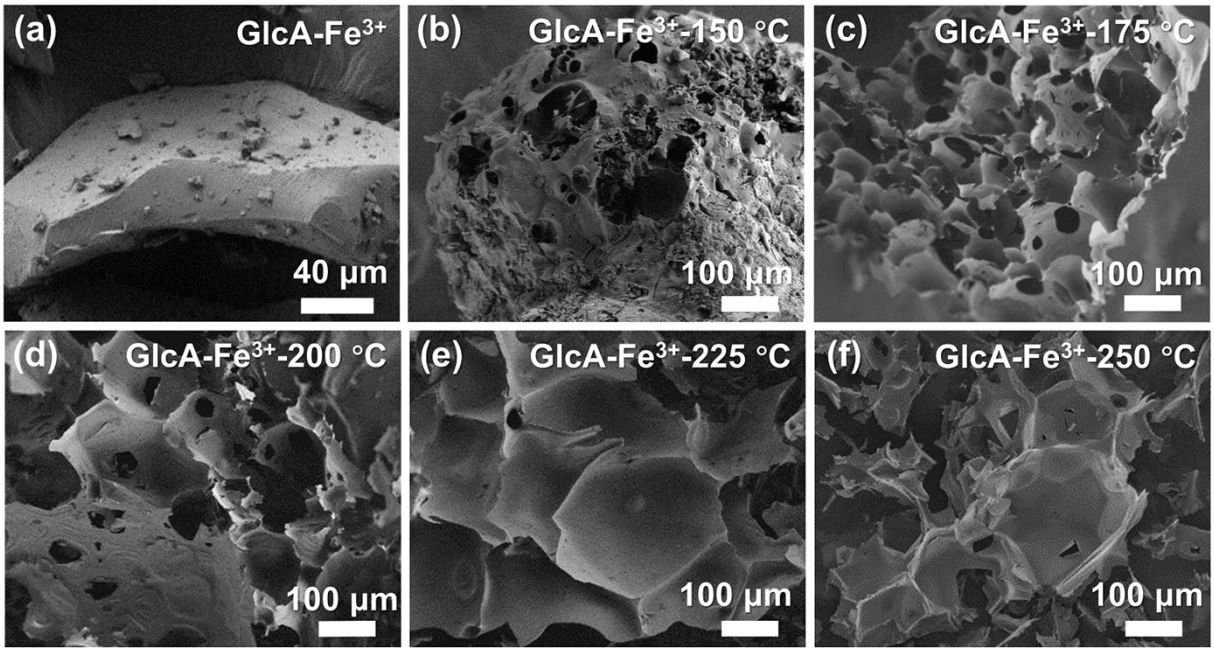

Figure S5. SEM images of GlcA-Fe^{3+} pyrolyzed at different temperatures: a) room temperature, b) 150 ℃, c) 175 ℃, d) 200 ℃, e) 225 ℃, and f) 250 ℃.

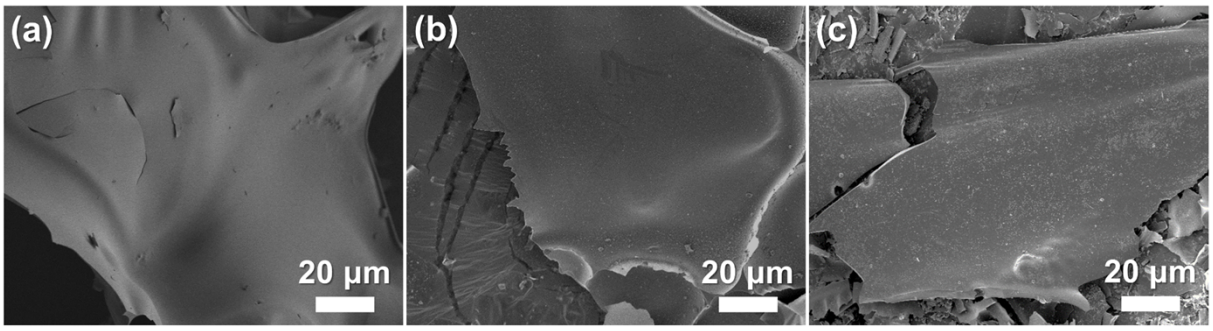

Figure S6. Low-resolution SEM images of a) Fe_3O_4/C-600, b) Fe_3O_4/C-700, and c) Fe_3O_4/C-800, respectively.

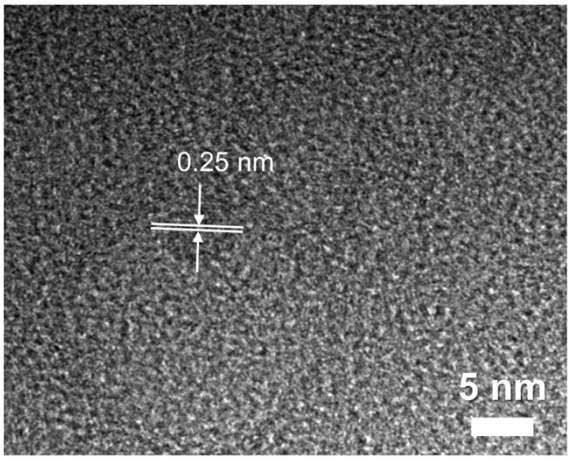

Figure S7. High-resolution TEM image of yolk-shell structure in the Fe_3O_4/C-700.

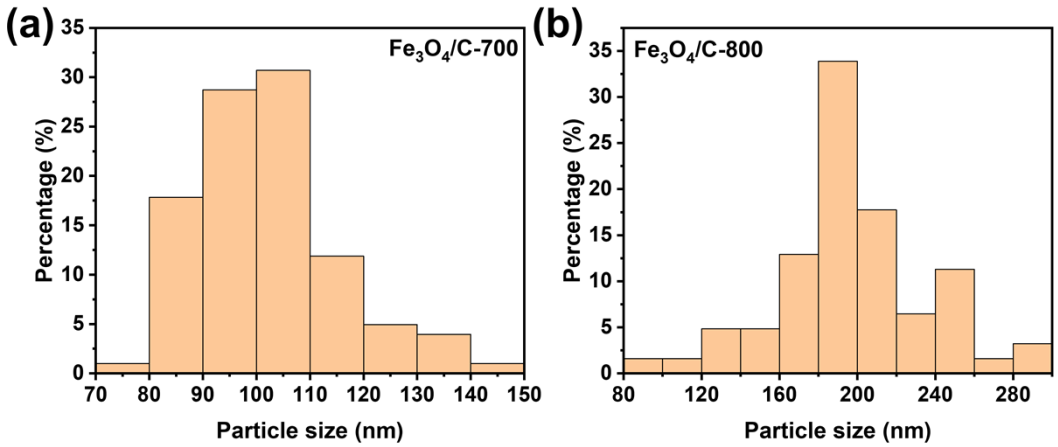

Figure S8. Size distributions of Fe_3O_4 nanocrystals for a) Fe_3O_4/C-700 and b) Fe_3O_4/C-800.

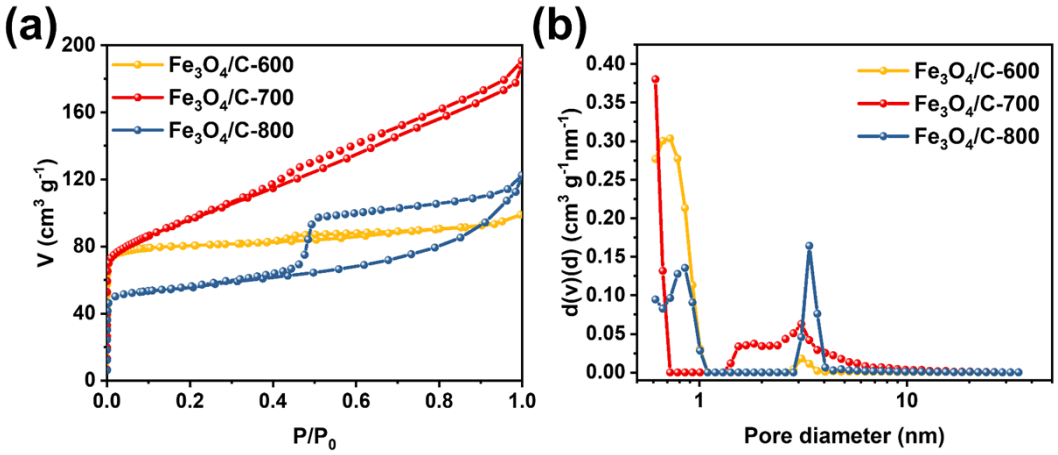

Figure S9. a) N_2 adsorption/desorption isotherms, and b) corresponding QSDFT pore-size distribution curves of Fe_3O_4/C at 600 °C, 700 °C, and 800 °C, respectively.

The specific surface area and pore structure characteristics of these Fe_3O_4/C composites are measured by N_2 adsorption/desorption isotherms (**Figure S9**). Due to the emergence of shell structures and the aggregation of Fe_3O_4 nanocrystals at 700 °C and 800 °C, much more mesopores and large pores will be produced. Thus, both Fe_3O_4/C-700 and Fe_3O_4/C-800 exhibit an enlarged hysteresis loop in a higher relative pressure range (P/P_0 of 0.4–0.99), comparing with Fe_3O_4/C-600. As displayed in **Figure S9b**, the corresponding pore size distributions are deduced by the QSDFT method, which validate that the Fe_3O_4/C-700 and Fe_3O_4/C-800 have abundant mesopores. More detailed pore parameters are listed in **Table S1**.

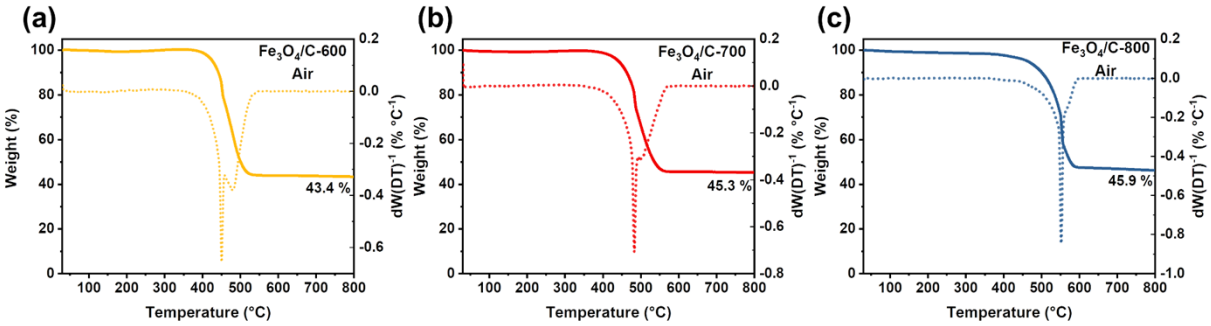

Figure S10. Thermogravimetric analysis (TGA) curve and derivative thermogravimetric (DTG) curve of a) Fe_3O_4/C-600, b) Fe_3O_4/C-700, and c) Fe_3O_4/C-800 under air atmosphere, respectively.

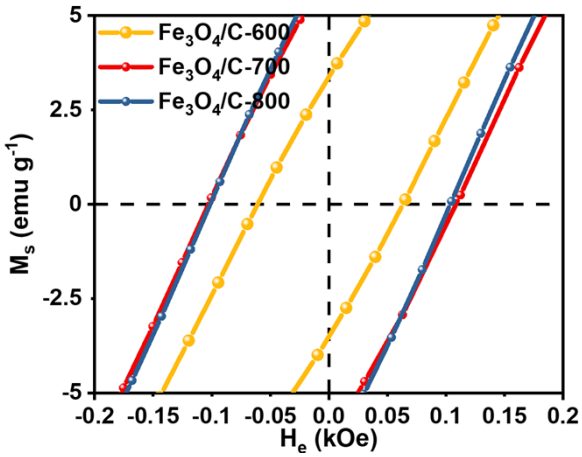

Figure S11. Magnified views of the hysteresis loop at low applied fields.

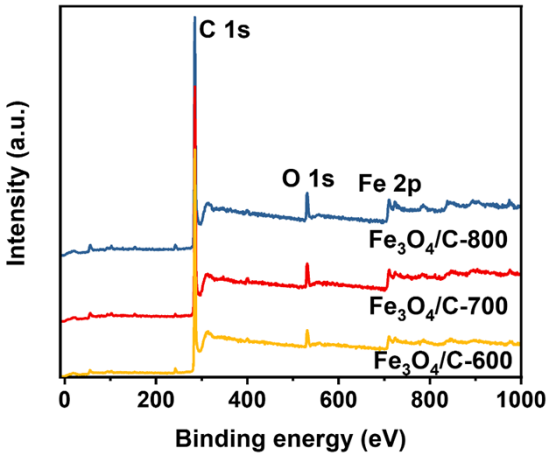

Figure S12. X-ray photoelectron spectroscopy (XPS) survey.

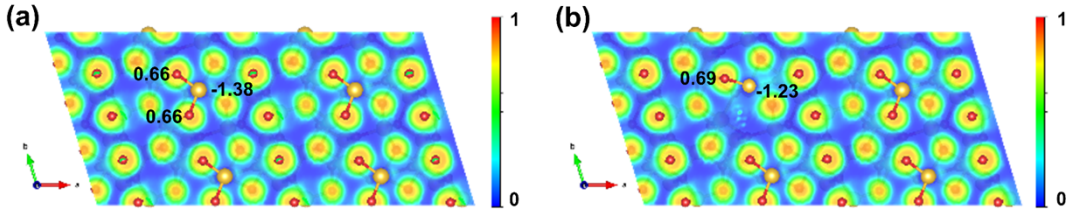

Figure S13. Calculated Bader charge: top view electron density differences of a) perfect Fe_3O_4 (311) plane and b) oxygen-vacancy Fe_3O_4 (311) plane.

The existence of oxygen vacancies in the Fe_3O_4 crystal results in the decrease of the electron loss of Fe atom from 1.38 to 1.23. The result agrees well with the negative shift of the binding energy of Fe element presented in XPS of Fe_3O_4/C-700 and Fe_3O_4/C-800.

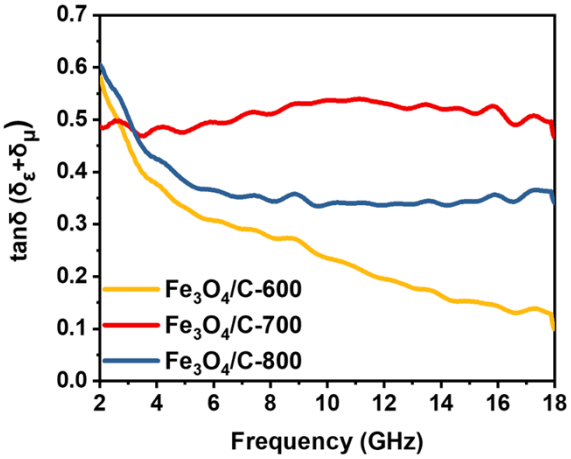

Figure S14. Loss factor (tanδ= tanδ_ε+tanδ_μ) of Fe_3O_4/C-600, Fe_3O_4/C-700, and Fe_3O_4/C-800, respectively.

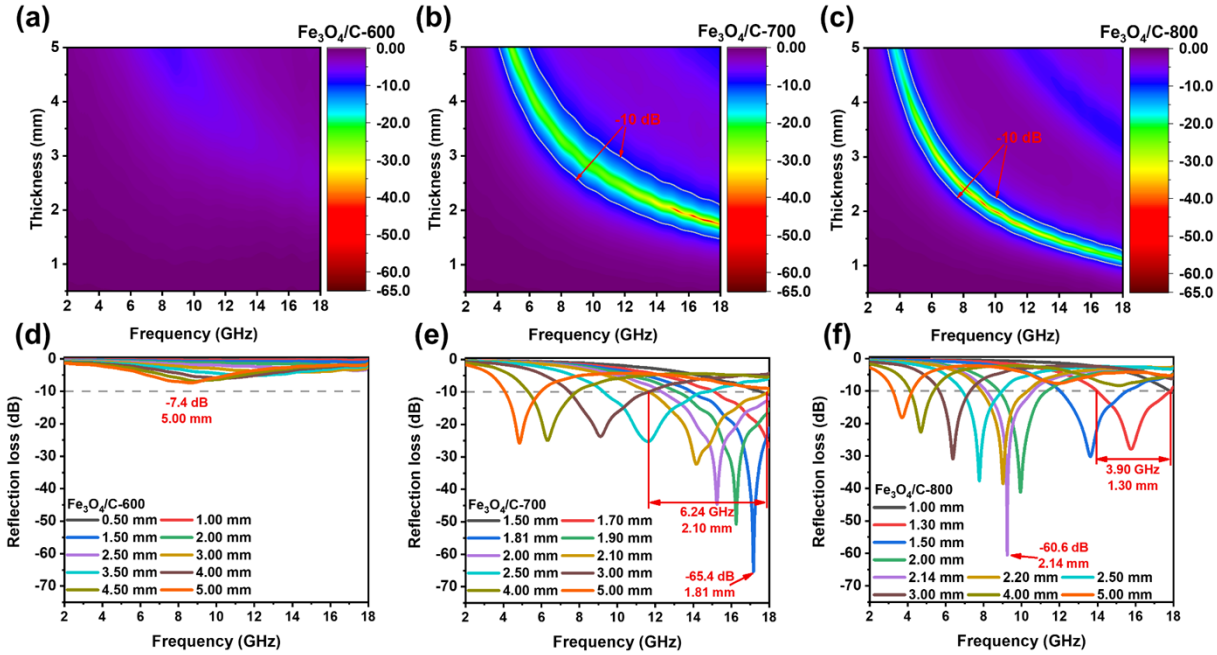

Figure S15. Reflection loss contour maps and corresponding curves of a) Fe_3O_4/C-600, b) Fe_3O_4/C-700, and c) Fe_3O_4/C-800, respectively.

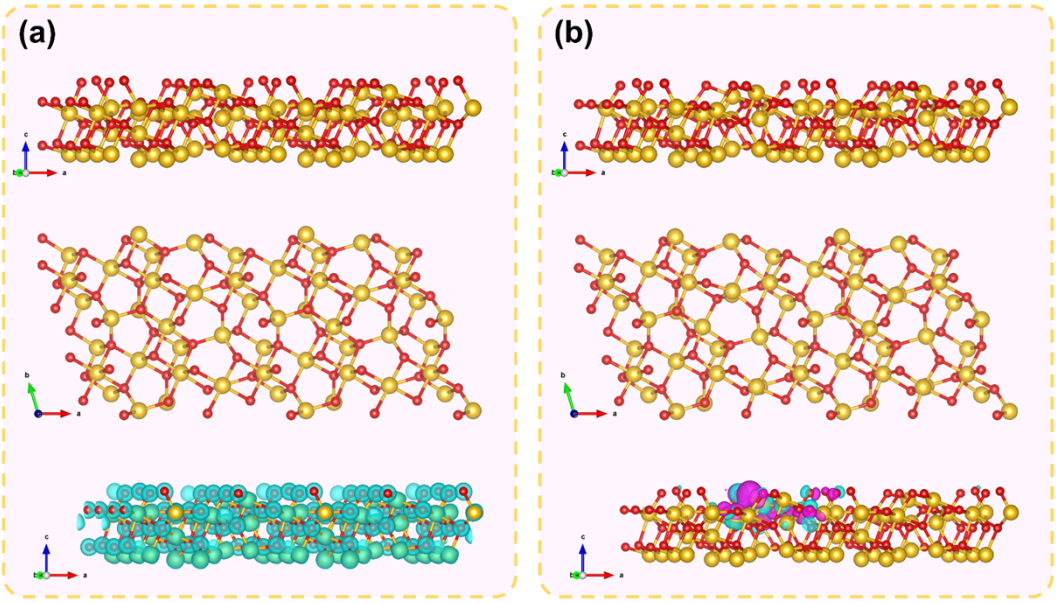

Figure S16. The side view (upper), top view (middle) and side view of charge distribution (bottom) of a) perfect Fe_3O_4 and b) oxygen-vacancy Fe_3O_4.

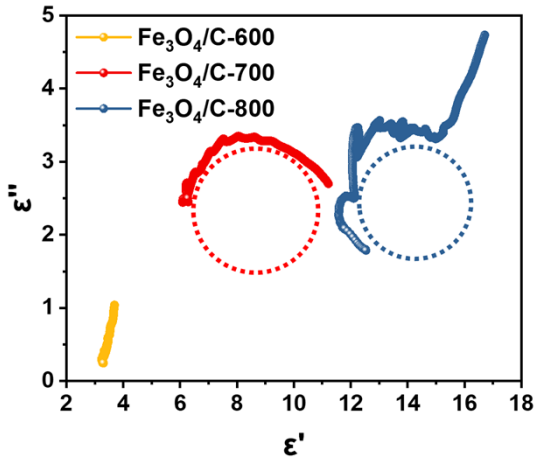

Figure S17. Cole-Cole plot of Fe_3O_4/C-600, Fe_3O_4/C-700, and Fe_3O_4/C-800, respectively.

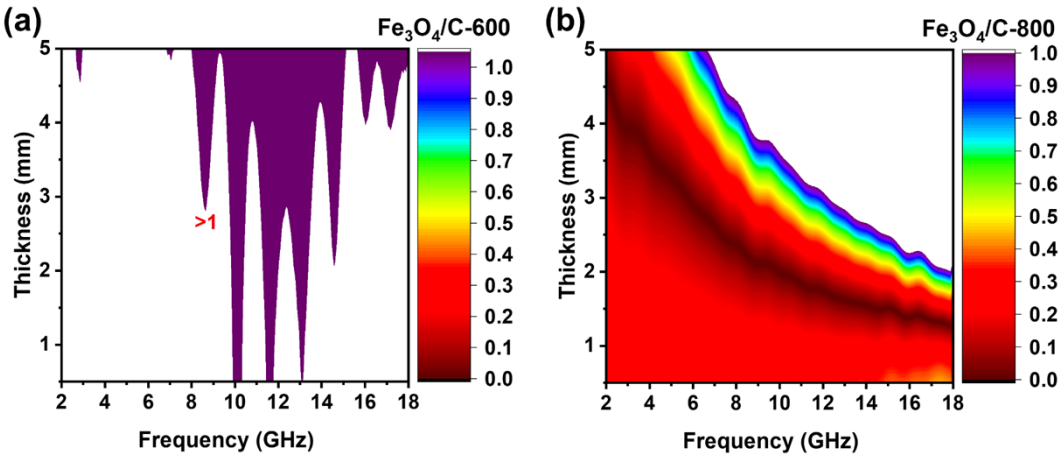

Figure S18. Calculated delta value maps of a) Fe_3O_4/C-600 and b) Fe_3O_4/C-800.

Table S1. Detailed pore parameters of Fe_3O_4/C-600, Fe_3O_4/C-700 and Fe_3O_4/C-800, respectively.

Sample	S_{BET} (m^2 g^{-1})	S_{Micro} (m^2 g^{-1})	V_{Total} (cm^3 g^{-1})	V_{Micro} (cm^3 g^{-1})
Fe_3O_4/C-600	296	272	0.15	0.11
Fe_3O_4/C-700	331	124	0.30	0.06
Fe_3O_4/C-800	179	113	0.19	0.06

Table S2. Comparison of EM wave absorption properties among Fe_3O_4/C-700 composite and other absorbers in recent literature.

Sample	Relection loss (dB)	Thickness (mm)	Effective absorption bandwidth (GHz)	References
Fe_3O_4/C-700	-65.4	1.81	6.24	This work
Ni/C	-57.25	1.8	5.1	[7]
SCN-16	-54.5	2.2	6.88	[8]
$ZnCo_2O_4$	-36.33	3.4	5.11	[9]
HBN-Co/C	-42.3	1.9	5.1	[10]
HCP@PANI	-64	2.5	5	[11]
FeNR@rGO	-23.09	4	3.9	[12]
BC/Fe_3O_4@C	-56.61	2.46	5.68	[13]
Co_3O_4@$NiCo_2O_4$	-34.42	2.3	4.88	[14]
Graphene@CuS	-54.5	2.5	4.5	[15]
Co/C	-35.3	4	5.8	[16]
NCO@CNTs	-45.1	2.5	2.7	[17]
Fe_3O_4/CF	-48.2	1.9	5.1	[18]
Fe_3O_4@CNS	-41.2	3	7.99	[19]
CMT@CNT/Co	-52.3	2	5.1	[20]
Co@NCNs	-60.6	2.4	5.1	[21]
Si_3N_4	-26.7	3.75	4.2	[22]
NiAl-LDH/G	-41.5	1.4	4.4	[23]
$Gd(OH)_3$@PPy	-51.4	2.2	4.8	[24]

References

1. Q. Song, F. Ye, L. Kong, Q. Shen, L. Han, L. Feng, G. Yu, Y. Pan and H. Li, *Adv. Funct. Mater.*, 2020, **30**, 2000475.
2. X. Zeng, X. Cheng, R. Yu and G. D. Stucky, *Carbon*, 2020.
3. M. Zhou, W. Gu, G. Wang, J. Zheng, C. Pei, F. Fan and G. Ji, *J. Mater. Chem. A*, 2020, **8**, 24267-24283.
4. R. Tandon, K. Sharma and N. Tandon, *Asian J. Chem.*, 2020, **32**, 3043-3046.
5. B. Han, W. Chu, X. Han, P. Xu, D. Liu, L. Cui, Y. Wang, H. Zhao and Y. Du, *Carbon*, 2020, **168**, 404-414.
6. N. Yang, R. Shao, Z. Zhang, M. Dou, J. Niu and F. Wang, *Carbon*, 2021, **178**, 775-782.
7. Y. Qiu, Y. Lin, H. Yang, L. Wang, M. Wang and B. Wen, *Chem. Eng. J.*, 2020, **383**, 123207.
8. B. Wen, H. Yang, Y. Lin, L. Ma, Y. Qiu and F. Hu, *J. Colloid Interface Sci.*, 2021, **586**, 208-218.
9. X. Li, L. Wang, W. You, L. Xing, X. Yu, Y. Li and R. Che, *Nanoscale*, 2019, **11**, 2694-2702.
10. J. Liang, J. Chen, H. Shen, K. Hu, B. Zhao and J. Kong, *Chem. Mater.*, 2021, **33**, 1789-1798.
11. X. Li, L. Yu, W. Zhao, Y. Shi, L. Yu, Y. Dong, Y. Zhu, Y. Fu, X. Liu and F. Fu, *Chem. Eng. J.*, 2020, **379**, 122393.
12. Y. Ding, L. Zhang, Q. Liao, G. Zhang, S. Liu and Y. Zhang, *Nano Res.*, 2016, **9**, 2018-2025.
13. Z. Li, H. Lin, S. Ding, H. Ling, T. Wang, Z. Miao, M. Zhang, A. Meng and Q. Li, *Carbon*, 2020, **167**, 148-159.
14. J. Wen, X. Li, G. Chen, Z. Wang, X. Zhou and H. Wu, *J. Colloid Interface Sci.*, 2021, **594**, 424-434.
15. P. Liu, Y. Huang, J. Yan, Y. Yang and Y. Zhao, *ACS Appl. Mater. Interfaces*, 2016, **8**, 5536-5546.
16. Y. Lü, Y. Wang, H. Li, Y. Lin, Z. Jiang, Z. Xie, Q. Kuang and L. Zheng, *ACS Appl. Mater. Interfaces*, 2015, **7**, 13604-13611.
17. Q. Hu, R. Yang, Z. Mo, D. Lu, L. Yang, Z. He, H. Zhu, Z. Tang and X. Gui, *Carbon*, 2019, **153**, 737-744.
18. Y. Liu, Z. Chen, W. Xie, S. Song, Y. Zhang and L. Dong, *ACS Sustain. Chem. Eng.*, 2019, **7**, 5318-5328.
19. Z. Liu, F. He, C. Shi, N. Zhao, E. Liu and C. He, *Chem. Phys. Lett.*, 2019, **716**, 221-226.
20. Z. Wu, K. Pei, L. Xing, X. Yu, W. You and R. Che, *Adv. Funct. Mater.*, 2019, **29**, 1901448.
21. P. Liu, S. Gao, G. Zhang, Y. Huang, W. You and R. Che, *Adv. Funct. Mater.*, 2021, 2102812.
22. F. Ye, Q. Song, Z. Zhang, W. Li, S. Zhang, X. Yin, Y. Zhou, H. Tao, Y. Liu and L. Cheng, *Adv. Funct. Mater.*, 2018, **28**, 1707205.
23. X. Xu, S. Shi, Y. Tang, G. Wang, M. Zhou, G. Zhao, X. Zhou, S. Lin and F. Meng, *Adv. Sci.*, 2021, **8**, 2002658.
24. W. Wei, X. Liu, W. Lu, H. Zhang, J. He, H. Wang and Y. Hou, *ACS Appl. Mater. Interfaces*, 2019, **11**, 12752-12760.